Geochemistry Geophysics Geosystems G3
AN ELECTRONIC JOURNAL OF THE EARTH SCIENCES
Published by AGU and the Geochemical Society

Article
Volume 6, Number 1
26 January 2005
Q01008, doi:10.1029/2004GC000813
ISSN: 1525-2027

Poroelastic damage rheology: Dilation, compaction, and failure of rocks

Yariv Hamiel
Institute of Earth Sciences, Hebrew University, Jerusalem 91904, Israel (yarivh@cc.huji.ac.il)

Also at Geological Survey of Israel, 30 Malkhe Yisrael Street, Jerusalem 95501, Israel

Vladimir Lyakhovsky
Geological Survey of Israel, 30 Malkhe Yisrael Street, Jerusalem 95501, Israel

Amotz Agnon
Institute of Earth Sciences, Hebrew University, Jerusalem 91904, Israel

[1] We present three-dimensional numerical simulations for the behavior of porous rocks under loading based on the theoretical formulation recently developed by Y. Hamiel et al. This theoretical formulation combines the classic Biot poroelastic theory with a damage rheology model. The numerical simulations of triaxial compression tests reproduce the gradual transition from localized brittle failure to distributed cataclastic flow with increasing pressure at high-porosity rocks. Under relatively low confining pressures (approximately lower than 100 MPa for Berea sandstone samples), porous rocks fail in a brittle mode with sharp localization of damage in a narrow deformation zone and dilatancy preceding the total failure. At these pressures the yield stress increases with confining pressure (positive slope for yield curve). In simulations with higher confining pressures, instead of dilatancy, the deformation zone has a reduced porosity due to compaction. The porosity reduction plays an essential role in strengthening the deformation zone, and therefore continuous loading of the sample leads to the progressive development of a wide deformation zone. Under relatively high confining pressures (approximately higher than 300 MPa for Berea sandstone samples), damage is nonlocalized, and the macroscopic deformation of the model corresponds to experimentally observed cataclastic flow. At these pressures the yield stress decreases with confining pressure (negative slope for yield curve). We found good agreement between the measured and calculated yield curve for Berea sandstone.

Components: 5429 words, 5 figures.

Keywords: damage rheology; numerical simulations; poroelasticity.

Index Terms: 5104 Physical Properties of Rocks: Fracture and flow; 8160 Tectonophysics: Rheology: general (1236, 8032); 3225 Mathematical Geophysics: Numerical approximations and analysis (4260).

Received 8 August 2004; **Revised** 11 November 2004; **Accepted** 11 December 2004; **Published** 26 January 2005.

Hamiel, Y., V. Lyakhovsky, and A. Agnon (2005), Poroelastic damage rheology: Dilation, compaction, and failure of rocks, *Geochem. Geophys. Geosyst.*, *6*, Q01008, doi:10.1029/2004GC000813.

1. Introduction

[2] Fracture process in low-porosity crystalline rocks is associated with sharp localization of microfracturing into a narrow fault zone [e.g., *Lockner et al.*, 1992], and with monotonic increase of the yield stress under increasing confining pressure. The fracture process in high-porosity rocks is considerably more complex, featuring different modes of failure ranging from brittle failure to cataclastic

flow [*Wong et al.*, 1997]. The mode of failure of high-porosity rocks strongly depends on the confining pressure. At low pressures, failure is associated with nucleation and dilation of microcracks and the rock fails along a localized deformation zone [*Lockner et al.*, 1992; *Wong et al.*, 1997]. With the increase of confining pressure, rather than dilating microcracks, shear bands are dominated by porosity loss due to compaction and grain crushing [*Menendez et al.*, 1996; *Wong et al.*, 1997]. The band material becomes mechanically stronger than the surrounding host rock, leading to a locking of developed bands and migration of the deformation. Therefore further increase of loading leads to a sequential development of a relatively wide shear zone. Such shear zones, often contain sets of narrow shear bands, and are widely observed in the field as well as in the laboratory [e.g., *Aydin and Johnson*, 1978; *Mair et al.*, 2000]. Under high pressures failure is accompanied by bulk sample compaction and transition to nonlocalized cataclastic flow [*Wong et al.*, 1997; *Wong and Zhu*, 1999]. The yield stress of high-porosity rocks at low pressures increases with pressure (positive slope for yield curve) until it achieves its maximal value at intermediate pressures. At relatively high pressures the yield stress decreases with pressure (negative slope for yield curve). This transition from positive to negative values of the slope is related to the different modes of failure in high-porosity rocks, i.e., transition from brittle failure to cataclastic flow [*Wong et al.*, 1997].

[3] Deformation and macroscopic failure of porous rocks have been simulated using several approaches. Among these are a discrete element model by *Place and Mora* [2000], a local degradation model by *Fang and Harrison* [2002], a viscoelastic damage rheology model for brittle failure by *Hamiel et al.* [2004b], and a discrete element model simulating a formation of pure compaction bands and cataclastic flow by *Katsman et al.* [2005]. A numerical model based on elastic damage mechanics that simulates the transition from localized to diffuse damage distribution has been proposed by *Amitrano et al.* [1999]. *Tang et al.* [2002] and *Rutqvist et al.* [2002] suggested a model for coupled analysis of flow, stress, and damage. *Shao* [1998] and *Bart et al.* [2000] proposed an anisotropic poroelastic damage model for saturated brittle porous materials to describe the main features related to the damage induced by microcracks, namely, deterioration of poroelastic properties, evolved anisotropy and dilatancy in the brittle regime. These models succeeded in simulating specific modes of failure of porous rocks. However, they came short of simulating the gradual transition from brittle failure to cataclastic flow including different modes of failure and the entire yield curve. Yielding of porous rocks, which includes brittle behavior at low pressures and semibrittle to cataclastic flow at higher pressures, is often modeled by an elastoplastic formulation [e.g., *Aydin and Johnson*, 1983; *Olsson*, 1999; *Issen and Rudnicki*, 2000; *Besuelle*, 2001]. However, this formulation does not account for fracture evolution and uses two independent yield surfaces: shear yield surface to describe failure at the brittle region; and compactive yield surface for the semibrittle and cataclastic flow region. Another rheological model that can describe the entire yield curve of high-porosity rocks by two independent yield surfaces (one for dilation, and one for compaction) is the two-phase viscous flow model suggested by *Ricard and Bercovici* [2003]. However, their model accounts for viscous rock deformation and leaves out elasticity. Recently, *Hamiel et al.* [2004a] proposed a new theoretical formulation that combines the classic Biot poroelastic theory [*Biot*, 1941] together with an isotropic damage model, and accounts for both elastic and inelastic processes. Their theoretical analysis based on the thermodynamic principles leads to a system of coupled kinetic equations for the evolution of damage and porosity. A significant advantage of the model is a particular emphasis on the brittle field and the ability to simulate the entire yield curve, positive as well as negative slopes, by a single formulation. In their model the transition from positive to negative values in the yield curve is determined by the competition between two thermodynamic forces: the force caused by damage change and the force caused by irreversible porosity change. For low effective pressures the force caused by damage change dominates (positive slope of the curve), whereas for high effective pressure the force caused by inelastic porosity change dominates (negative slope).

[4] In this paper we present results of three-dimensional numerical simulations of porous rock deformation and failure, using the theoretical formulation developed by *Hamiel et al.* [2004a]. The numerical simulations presented here reproduce the gradual transition from brittle failure to cataclastic flow at high-porosity rocks.

2. Poroelastic Damage Model

[5] In this section we briefly summarize the main features of the poroelastic damage model (for

detailed derivation of the governing equations, see *Hamiel et al.* [2004a]). Rock deformation is associated with the formation and growth of internal flaws. From a mechanical point of view, these flaws can be divided into two classes: pores and microcracks in the matrix of the porous rock. Microcracks act as high-stress concentrators and hence respond readily to loading leading to brittle failure. Pores are stiffer than microcracks and associated with minor stress variations, contributing to cataclastic flow. For a system with a sufficiently large number of cracks and pores, one can define a representative volume in which the flaw density is uniform and introduce an intensive damage variable (α) and porosity (ϕ) for this volume. The damage variable α is responsible for the change in material stiffness due to microcracking or healing. An overall damage-related change of volumetric deformation after complete unloading is assumed negligibly small. Material porosity is the volume fraction of pores after complete unloading and changes in this variable refer to inelastic change in the pore volume.

[6] Following Biot's theory of poroelasticity [*Biot*, 1941, 1956] the free energy of a poroelastic medium, F, is a sum of the elastic energy and the poroelastic coupling term of the saturated medium:

$$F = \frac{\lambda(\alpha,\phi)}{2} I_1^2 + \mu(\alpha,\phi) I_2 - \gamma(\alpha,\phi) I_1 \sqrt{I_2} + \frac{1}{2} M \cdot [\beta I_1 - (\zeta - \phi)]^2, \quad (1)$$

This energy is a function of two invariants of the elastic strain ϵ_{ij} ($I_1 = \epsilon_{kk}$; $I_2 = \epsilon_{ij}\epsilon_{ij}$, index summation convention is assumed), fluid volume content, ζ, material porosity, ϕ, and damage variable, α. Following *Lyakhovsky et al.* [1997], who defined the elastic energy for nonlinear damaged media, the elastic energy under drained conditions (constant fluid pressure) includes two Hookean terms with the Lame drained moduli λ, μ, and an additional nonlinear term with strain coupling modulus γ. M and β are the Biot modulus and Biot's coefficient for porous media.

[7] Differentiation of the poroelastic energy (1) leads to constitutive relations for the stress tensor, σ_{ij}, and fluid pressure, p:

$$\sigma_{ij} = \frac{\partial F}{\partial \varepsilon_{ij}} = \left(\lambda - \frac{\gamma}{\xi}\right) I_1 \delta_{ij} + (2\mu - \gamma\xi)\varepsilon_{ij} + \beta M[\beta I_1 - (\zeta - \phi)]\delta_{ij}, \quad (2)$$

$$p = \frac{\partial F}{\partial \zeta} = M[-\beta I_1 + (\zeta - \phi)], \quad (3)$$

where $\xi = I_1/\sqrt{I_2}$ is the strain invariant ratio changing from $\xi = -\sqrt{3}$ for isotropic compaction to $\xi = \sqrt{3}$ for isotropic dilation. The effect of rock degradation is simulated by making the poroelastic moduli functions of the damage variable. In the general case, the poroelastic moduli are functions of the material porosity, ϕ, and the damage variable, α [*Hamiel et al.*, 2004a]. However, in the simulations presented in this paper, the material porosity change within a few presents (between 18–21%) and the direct effect of the porosity on the elastic moduli is negligible. Therefore the elastic moduli μ and γ are assumed to depend only on the damage variable α. Following *Agnon and Lyakhovsky* [1995] and *Hamiel et al.* [2004a], we use linear approximations:

$$\mu(\alpha) = \mu_0 + \xi_0 \gamma_1 \alpha \qquad \gamma(\alpha) = \gamma_1 \alpha \quad (4)$$

where μ_0, γ_1, and ξ_0 are constants for each material. The coefficient ξ_0 is related to the friction angle [*Agnon and Lyakhovsky*, 1995], and the moduli μ_0, γ_1 are constrained by the conditions for loss of convexity (equations (14) and (15) of *Lyakhovsky et al.* [1997]). Nonlinear, power law relations between the elastic moduli and the damage are discussed by *Hamiel et al.* [2004b].

[8] Material porosity and damage evolve with time as a result of the ongoing deformation. Using the balance equations of the energy and entropy, Gibbs relation, fluid mass conservation equation, the definitions of the stress tensor (2), and fluid pressure (3), *Hamiel et al.* [2004a] derived the local entropy production Φ related to kinetics of porosity and damage:

$$\Phi = -\frac{\partial F}{\partial \alpha}\frac{d\alpha}{dt} - P_e \frac{d\phi}{dt} \geq 0. \quad (5)$$

We have introduced in (5) the effective pressure $P_e = \frac{-\sigma_{kk}}{3} - p$ (mean stress minus fluid pressure). The first term in equation (5) is related to kinetics of damage and the second term is related to porosity change. In the case of fracturing ($d\alpha/dt > 0$) and dilation ($d\phi/dt > 0$), dominant under relatively low pressures, the first term is positive and associated with dissipation, while the second term is negative and acts as a storage of energy. This balance may be viewed as partitioning of free energy between heat and stored surface energy associated with increased porosity. The thermodynamic formulation provides a self-consistent energy partitioning. An alternative approach, with appropriate assumptions on the

ratio between heat and surface energy terms, was presented recently [*Bercovici and Ricard*, 2003]. In order to assure nonnegativity of the local entropy production Φ, we write the phenomenological equations for the kinetics of α and ϕ as a set of two coupled differential equations [*deGroot and Mazur*, 1962; *Malvern*, 1969]

$$\begin{aligned} \frac{d\phi}{dt} &= -C_1 P_e - C_2 \frac{\partial F}{\partial \alpha} \\ \frac{d\alpha}{dt} &= C_2 P_e - C_3 \frac{\partial F}{\partial \alpha} \end{aligned}, \tag{6}$$

where C_1, C_2, C_3 are positive kinetic coefficients. Each term in the kinetic equations (6) represents a thermodynamic force; one relates to damage ($\partial F/\partial\alpha$) and one to porosity change (P_e). The terms with the kinetic coefficients C_1 and C_3 are respectively responsible for the evolution of α and ϕ as functions of damage- and porosity-related forces, while the coefficient C_2 is responsible for the coupling between the kinetics of damage and porosity. The competition between these forces reproduces the different modes of failure in porous rocks. Using the poroelastic energy (1) and the connection between the elastic moduli and the damage variable α (4), the kinetic equation (6) can be rewritten as:

$$\frac{d\phi}{dt} = -C_1 P_e + C_2 \gamma_1 I_2(\xi - \xi_0) \tag{7a}$$

$$\frac{d\alpha}{dt} = C_2 P_e + C_3 \gamma_1 I_2(\xi - \xi_0). \tag{7b}$$

Following the Hertzian contact theory, *Hamiel et al.* [2004a] suggested that C_2 is a power law expression of the effective pressure, $C_2 = DP_e^n$. They demonstrated that the transition from positive to negative values of the slope of the yield curve (yield cap) is a general feature of the model for $n > 1$, and estimated $D \sim 10^{-10}$ MPa^{-3} s^{-1} and $n = 2$ for sandstones. They also show that C_1 is in the order of 10^{-18}–10^{-22} 1/(Pa s), and therefore is negligibly small for laboratory timescale. *Lyakhovsky et al.* [1997] and *Hamiel et al.* [2004b] used results of laboratory experiments to constrain the coefficient of damage rate, C_3. They found that C_3 on the order of $0.5/\gamma_1$ to $10/\gamma_1$ (Pa s)$^{-1}$ provided a good fit to observed data for damage increase. *Hamiel et al.* [2004a] presented sensitivity analysis of the yield curve to the different model coefficients. Motivated by the observed logarithmic increase of the static coefficient of friction with time, *Lyakhovsky et al.* [1997] used a damage-dependent function for the kinetics of damage decrease (healing) of the form:

$$C_3(\alpha) = A_1 \cdot \exp\left(\frac{\alpha}{A_2}\right) \text{ for } \frac{d\alpha}{dt} < 0, \tag{8a}$$

where A_1 and A_2 are constants describing the rate of healing. The analytical and numerical results of V. Lyakhovsky et al. (A visco-elastic damage rheology and rate- and state-dependent friction, submitted to *Geophysical Journal International*, 2004) provide quantitative connections between kinetic parameters A_1 and A_2 of the damage rheology model and the parameters a and b of rate- and state-dependent friction. Laboratory experiments [*Olsen et al.*, 1998; *Tenthorey et al.*, 2003] reveal the strong connection between material strengthening and grain crushing and compaction in high-porosity rocks. To account for this porosity-related enhancement of material healing the kinetic coefficient C_3 is rewritten as:

$$C_3(\alpha,\phi) = \begin{cases} \text{const.} & \text{for } \dfrac{d\alpha}{dt} \geq 0 \\ A_1 \cdot \exp\left(\dfrac{\alpha}{A_2}\right) \cdot \exp(B(\phi_0 - \phi)) & \text{for } \dfrac{d\alpha}{dt} < 0 \end{cases}, \tag{8b}$$

where ϕ_0 is the initial porosity. Thus the damage rate coefficient for material healing is now a function of both damage variable and material porosity.

[9] The above formulation of the poroelastic damage model can be reduced to the classic formulation developed by *Biot* [1941, 1956] for linear poroelastic media in the limit of zero damage intensity ($\alpha = 0$) and at the same time can be reduced to the model derived by *Lyakhovsky et al.* [1997] for damaged elastic media with vanishing fluid pressure ($p = 0$).

3. Numerical Method

[10] Numerical simulation is aimed at reproducing standard triaxial rock mechanics tests with high-porosity samples. Simulations are run with constant confining pressures from 25 to 400 MPa, with strain rate 5×10^{-5} s^{-1}. The sample has a rectangular shape with aspect ratio 1:2 between horizontal and vertical size. In these simulations we used the following mechanical properties of the rock: $\lambda = 7 \times 10^3$ MPa; $\mu_0 = 1.8 \times 10^4$ MPa; $\xi_0 = -0.8$ corresponding to internal friction angle $\phi = 65°$; Biot modulus $M = 1.5 \times 10^4$ MPa; Biot coefficient $\beta = 1$; initial porosity $\phi_0 = 20\%$;

corresponding to the properties of the Berea sandstone measured in the laboratory experiments [*Lockner et al.*, 1992]. In agreement with previous estimations [*Hamiel et al.*, 2004a, 2004b] we used the following kinetic coefficients in equations (7) and (8): $C_1 = 0$; $D = 4 \times 10^{-11}$ MPa^{-3} s^{-1} and $n = 2$; $C_3 = 7/\gamma_1$ (Pa s)$^{-1}$, for weakening ($d\alpha/dt > 0$), and $A_1 = 10^{-2}/\gamma_1$ (Pa s)$^{-1}$, $A_2 = 0.1$, $B = 500$ for healing ($d\alpha/dt < 0$). Small, initial random distribution of damage ($\alpha < 0.1$) reproduces initial heterogeneity of the sample. Constant fluid pressure of $p = 5$ MPa was set along all of the boundaries to mimic drained conditions. In order to avoid boundary effects, a thin undamaged layer with constant porosity (20%) was set at the top and bottom boundaries of the sample.

[11] The general numerical procedure involves solving the following equations: force balance equation

$$\frac{\partial \sigma_{ij}}{\partial x_j} = 0, \tag{9}$$

Darcy's law coupled with fluid mass conservation equation, with constant hydraulic conductivity, $\kappa = 10^{-12}$ m^2/(Pa s)

$$\frac{\partial \zeta}{\partial t} = \kappa \cdot \nabla^2 p, \tag{10}$$

and the constitutive relations (2) and (3). The evolving elastic moduli $\mu(\alpha)$, $\gamma(\alpha)$ and porosity ϕ are calculated using the kinetic equations (7a) and (7b) with variable healing rate coefficient C_3(8b). All the equations are solved using explicit-in-time scheme following the Fast Lagrangian Analysis of Continua (FLAC) algorithm [*Cundall and Board*, 1988; *Cundall*, 1989; *Poliakov et al.*, 1993]. Using an updated Lagrangian scheme provides the capability for large strains. Inertial terms are included in the equilibrium equations are rewritten in the form

$$\frac{\partial v_i}{\partial t} = \frac{F_i}{m}, \tag{11}$$

where v_i and F_i are velocity and force applied to a node of mass m. This allows simulating physical instability without numerical instability. The node forces are calculated by integrating the stresses across all the surfaces S of the elements adjusted to the grid point

$$F_i = \oiint_S \sigma_{ij} n_j dS. \tag{12}$$

The solution of equations (10)–(12) provides velocities at each grid point, which are used to calculate element strains and fluid content. These strains and fluid content substituted into constitutive relations (2) and (3) provide element stresses and fluid pressure. These forces recalculated to the grid nodes (12) are the necessary input for the solution of the equation of motion in the next step of the calculation cycle.

[12] The damage variable (α) and porosity (ϕ) for each element is calculated for every numerical cycle according to the kinetic equations (7) with numerical time step defined by adaptive procedure [*Lyakhovsky et al.*, 2001]. Every change in the damage and porosity leads to a corresponding change in the effective elastic moduli and fluid pressure in the element. This change affects the stress field in the surrounding area through the solution of force balance equation (9) and Darcy law (10). If damage in one element achieves its critical level ($\alpha = \alpha_{cr}$) then a stress drop occurs. The real dynamic process, wherein the stress drop generates waves, is not simulated here. However, a quasi-dynamic procedure is applied to simulate a rupture front propagation. This is accomplished by recalculating the stress field after each stress drop for every element involved in the rupture process.

4. Simulation Results

[13] In this section we present the results of numerical simulations of standard triaxial tests with constant confining pressures starting from 25 up to 400 MPa. The set of simulations allows investigating model behavior under various pressures and reproducing the transition from brittle failure to cataclastic flow anticipated from the analysis of *Hamiel et al.* [2004a]. The numerical simulations further allow visualizing the transition from localized to nonlocalized damage and porosity distributions. Yielding (occasionally termed first yielding) in our model is related to onset of damage increase. This relation is in agreement with the experimental observations on rapid increase in acoustic emission after exceeding the yield stress [*Zhang et al.*, 1990; *Wong et al.*, 1997]. Figure 1 shows the calculated yield stress from the numerical simulations. The shape of the calculated yield curve is determined by the competition between the first and second terms in the equation for damage evolution (7b). For low effective pressures the second term is dominant, causing a positive slope of the curve, whereas for high effective pressures the first term becomes dominant, causing a negative slope. Also

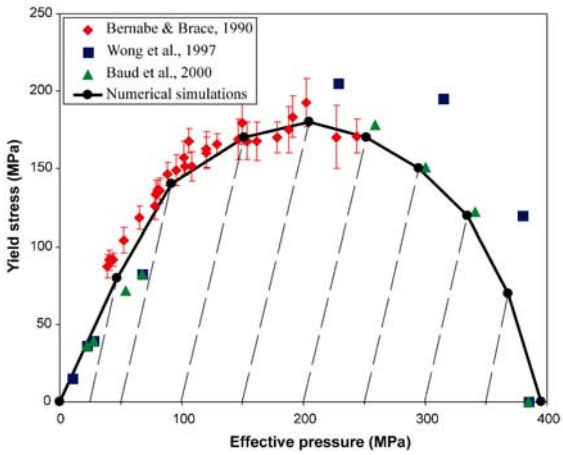

Figure 1. Experimentally measured yield stress for Berea sandstone compared with calculated curve from the numerical simulations. Symbols indicate experimental results from *Bernabe and Brace* [1990], *Wong et al.* [1997], and *Baud et al.* [2000]. Dashed lines indicate the numerical loading path from the beginning of the modeling with zero differential stress up to the yield stress. The black circles indicate the yield stress from the numerical simulations.

shown in Figure 1 are the experimentally measured yield stresses for Berea sandstone from *Bernabe and Brace* [1990], *Wong et al.* [1997], and *Baud et al.* [2000]. The measured values of yield stress for Berea sandstone samples show significant scattering between data sets at high pressures reported by different authors. Thus the calculated yield curve cannot fit all the presented data sets at high pressures simultaneously. The calculated yield curve provides a reasonable fit to the experimentally measured yield stress for Berea sandstone at high pressures reported by *Baud et al.* [2000]. The experimental data under high pressures reported by *Wong et al.* [1997] could also be fitted with the present model with a higher value of the power n in the expression for C_2 (not shown here). Several simulated stress-strain curves are shown in Figure 2. At relatively low confining pressures the inelastic porosity change (equation (7a)) is negligibly small until yielding and stress-strain curves are linear in this regime (blue and red curves for 50 or 100 MPa, respectively). The stress-strain curves start to deviate from a straight line, predicted by linear poroelasticity, only when damage starts to accumulate. In this case the yield stress can be determined directly from the stress-strain curves, as reported by *Bernabe and Brace* [1990] from the laboratory experiments with Berea sandstone at relatively low pressures. At high pressures the inelastic compaction is significant, even before the onset of damage, and the stress-strain curves become nonlinear well before the yield stress (green and orange curves for 300 and 350 MPa in Figure 2). The yield stress first increases with pressure (blue and red curves for 50 and 100 MPa, respectively) and then decreases at high confining pressures (green and orange curves for 300 and 350 MPa, respectively). This is in agreement with the yield cap (Figure 1). In contrast to the simulations with low pressures, the stress drop after the peak stress at high pressures is very small or does not exist at all. The overall behavior of the simulations with high confining pressure corresponds to experimentally observed cataclastic flow [*Menendez et al.*, 1996; *Wong et al.*, 1997]. As in the laboratory results, the sample has a barrel-like shape and both damage and porosity are nonlocalized, with nearly homogeneous distribution throughout the sample (not shown here).

[14] The simulated transition from brittle failure to cataclastic flow is controlled by confining pressure similar to laboratory experimental results. Figures 3 and 4 present results of damage and porosity distribution during simulations with relatively low (50 and 100 MPa), confining pressures. In both cases the damage and porosity distributions are significantly heterogeneous. The deformation is much more localized and the barreling effect is small, especially at 50 MPa confining pressure. Figures 3 and 4 demonstrate four snapshots corresponding to different stages of the fracture zone evolution: nucleation (snapshot I), in-plane propagation (snapshot II), total failure (snapshot

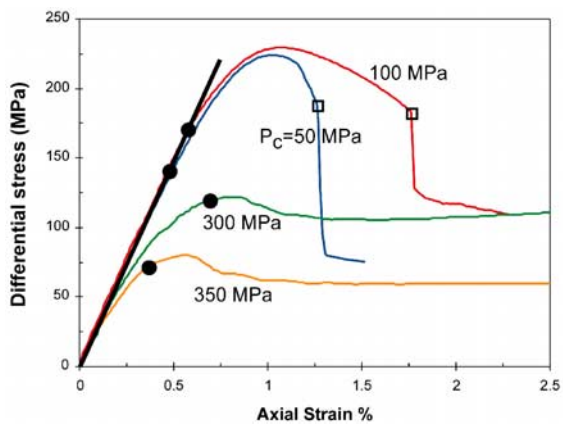

Figure 2. Differential stress versus axial strain from the simulations with 50 (blue), 100 (red), 300 (green), and 350 (orange) MPa confining pressure. The yield stress (or onset of damage) is indicated by black dots. The black line represents stress-strain relations expected from linear poroelasticity. Open squares indicate the initial stage of nucleation of a deformation zone with porosity reduction above 2%.

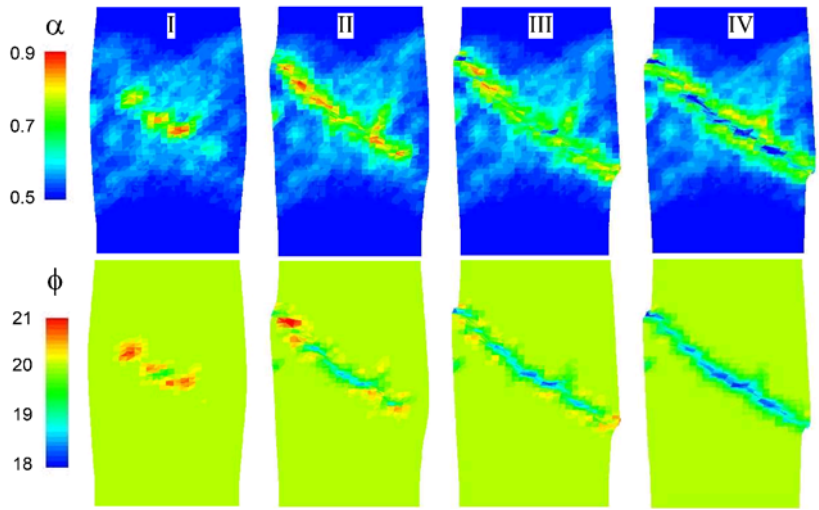

Figure 3. Four snap shots (I–IV), representing four stages of rock-sample deformation during triaxial test simulation with 50 MPa confining pressure and 20% initial porosity. Each stage is represented by the damage variable (α) distribution (upper snap shots) and the porosity (ϕ) distribution (lower snap shots).

III), and sliding and out-of-plane growth (snapshot IV). During the nucleation stage at 50 MPa confining pressure (Figure 3) the fracture zone is dilated and the inelastic porosity increases, while at 100 MPa confining pressure (Figure 4) there is no dilatancy, and failure is preceded by compaction and porosity loss. During the next stages the compaction of a newly created damage zone leads to porosity-enhanced healing (equation (8b)). This effect is much more efficient at 100 MPa than at 50 MPa, due to the higher compaction at 100 MPa. The strengthening of the compacted rock inside the deformation zone leads to damage increase outside the deformation zone and to the progressive development of a wide deformation zone. Therefore the deformation zone is localized through the loading at 50 MPa, and continuously widens at 100 MPa. Figure 5 presents the width of the deformation zone normalized to the sample length for the simulations with 50 and 100 MPa confining pressure. The deformation zone width refers to the region whose initial porosity of 20% is reduced by more than 2%. The strain in Figure 5 is counted from the first appearance of an element compacted by more than 2%. This point is marked by open squares in Figure 2. The choice of 2% for compaction of the deformation zone is arbitrary and does not effect the general relations between the strain and the width of the deformation zone. At 100 MPa confining pressure the width of the deformation zone increases

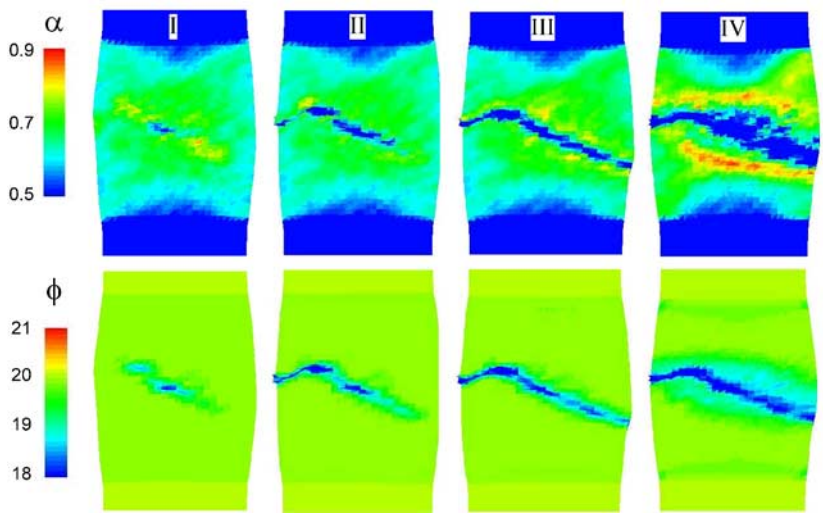

Figure 4. The same as Figure 3, for a simulation with 100 MPa confining pressure.

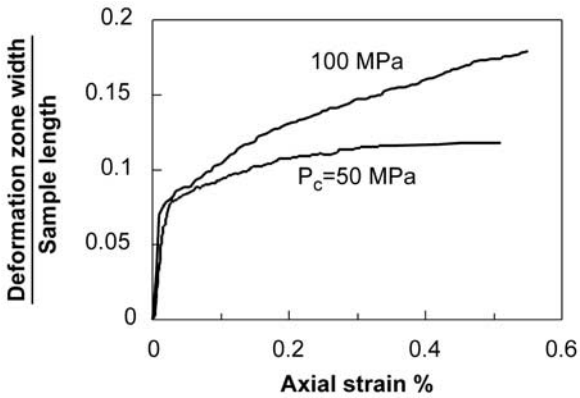

Figure 5. Normalized width of a deformation zone versus axial strain for the simulations with 50 and 100 MPa confining pressures. Deformation zone refers to a zone in which the initial porosity of 20% is reduced by more than 2%. The strain is counted from the initial stage of nucleation of deformation zone (open squares in Figure 2).

almost linearly with axial strain, while at 50 MPa the deformation zone width stays almost constant. The numerical model also predicts different spatial orientation of the deformation zone. The angle between the direction of the deformation zone and the maximum compressive stress is approximately 45° at 50 MPa (Figure 3), whereas at 100 MPa this angle is about 65°. These model predictions of the evolution and orientation of the deformation zones at relatively low and intermediate confining pressures are in agreement with observations from experiments on sandstone samples [*Bernabe and Brace*, 1990; *Mair et al.*, 2000; *Besuelle*, 2001].

5. Conclusions

[15] We have presented numerical simulations that confirm theoretical predictions and allow calibrating of the damage poroelastic model of *Hamiel et al.* [2004a]. In agreement with theoretical analysis of the thermodynamic forces related to porosity change and microcracking, the numerical model reproduces different modes of macroscopic failure for high-porosity rocks. At low confining pressures, rocks fail in a brittle mode, with strong damage localization in a narrow deformation zone. The thermodynamic force related to microcracking is dominant and the yield stress increases with confining pressure (positive slope for yield curve). During the nucleation stage at relatively low confining pressure the fracture zone is dilated and the inelastic porosity increases, while at intermediate confining pressure there is no dilatancy, and failure is preceded by compaction and porosity loss. At intermediate confining pressure strengthening of the compacted rock inside the deformation zone leads to the sequential development of a wide deformation zone. The role of porosity-related thermodynamic force increases with increasing confining pressure, leading to decrease of yield stress with confining pressure (negative slope for yield curve). At high confining pressures damage is nonlocalized and the macroscopic deformation of the model corresponds to experimentally observed cataclastic flow. The development provides an internally consistent framework for simulating gradual transition from brittle fracture to cataclastic flow in high-porosity rocks and coupled evolution of fractures and fluid flow in a variety of practical geological and engineering problems such as earthquakes, nucleation of deformation features and fluid flow during seismic cycles.

Acknowledgments

[16] We thank Magali Billen and two anonymous reviewers for their constructive reviews. Y. Hamiel and V. Lyakhovsky gratefully acknowledge the support from the US-Israel Binational Science Foundation, grant BSF-9800198. V. Lyakhovsky is thankful for the support of ISF 479/03, and A. Agnon for the support of EU-INTAS grant 0748.

References

Agnon, A., and V. Lyakhovsky (1995), Damage distribution and localization during dyke intrusion, in *The Physics and Chemistry of Dykes*, edited by G. Baer and A. Heimann, pp. 65–78, A. A. Balkema, Brookfield, Vt.

Amitrano, D., J. R. Grasso, and D. Hantz (1999), From diffuse to localized damage through elastic interaction, *Geophys. Res. Lett.*, *26*, 2109–2112.

Aydin, A., and A. M. Johnson (1978), Development of faults as zones of deformation bands and as slip surfaces in sandstone, *Pure Appl. Geophys.*, *116*, 931–942.

Aydin, A., and A. M. Johnson (1983), Analysis of faulting in porous sandstones, *J. Struct. Geol.*, *5*, 19–31.

Bart, M., J. F. Shao, and D. Lydzba (2000), Poroelastic behavior of saturated brittle rock with anisotropic damage, *Int. J. Numer. Anal. Methods Geomech.*, *24*, 1139–1154.

Baud, P., W. Zhu, and T. Wong (2000), Failure mode and weakening effect of water on sandstone, *J. Geophys. Res.*, *105*, 16,371–16,389.

Bercovici, D., and Y. Ricard (2003), Energetics of a two-phase model of lithospheric damage, shear localization and plate-boundary formation, *Geophys. J. Int.*, *152*, 581–596.

Bernabe, Y., and W. F. Brace (1990), Deformation and fracture of Berea sandstone, in *The Brittle-Ductile Transition in Rocks*, *Geophys. Monogr. Ser.*, vol. 56, edited by A. G. Duba et al., pp. 91–101, AGU, Washington, D. C.

Besuelle, P. (2001), Compacting and dilating shear bands in porous rock: Theoretical and experimental conditions, *J. Geophys. Res.*, *106*, 13,435–13,442.

Biot, M. A. (1941), General theory of three-dimensional consolidation, *J. Appl. Phys.*, *12*, 155–164.

Biot, M. A. (1956), General solutions of the equations of elasticity and consolidation for a porous material, *J. Appl. Mech.*, *78*, 91–96.

Cundall, P. A. (1989), Numerical experiments on localization in frictional materials, *Ing. Arch.*, *59*, 148–159.

Cundall, P. A., and M. Board (1988), A microcomputer program for modeling large-strain plasticity problems, in *Numerical Methods in Geomechanics, Proceedings 6th International Conference on Numerical Methods in Geomechanics, Innsbruck*, edited by C. Swoboda, pp. 2101–2108, A. A. Balkema, Brookfield, Vt.

deGroot, S. R., and P. Mazur (1962), *Nonequilibrium Thermodynamics,* Elsevier, New York.

Fang, Z., and J. P. Harrison (2002), Development of a local degradation approach to the modeling of brittle fracture in heterogeneous rocks, *Int. J. Rock Mech. Min. Sci.*, *39*, 443–457.

Hamiel, Y., V. Lyakhovsky, and A. Agnon (2004a), Coupled evolution of damage and porosity in poroelastic media: Theory and applications to deformation of porous rocks, *Geophys. J. Int.*, *156*, 701–713.

Hamiel, Y., Y. Liu, V. Lyakhovsky, Y. Bien-Zion, and D. A. Lockner (2004b), A visco-elastic damage model with applications to stable and unstable fracturing, *Geophys. J. Int.*, *159*, 1155–1165.

Issen, K. A., and J. W. Rudnicki (2000), Conditions for compaction bands in porous rock, *J. Geophys. Res.*, *105*, 21,529–21,536.

Katsman, R., E. Aharonov, and H. Scher (2005), Numerical simulation of compaction bands in high-porosity sedimentary rock, *Mech. Mater.*, *37*(1), 143–162.

Lockner, D. A., J. D. Byerlee, V. Kuksenko, A. Ponomarev, and A. Sidorin (1992), Observations of quasi-static fault growth from acoustic emissions, in *Fault Mechanics and Transport Properties of Rocks*, *Int. Geophys. Ser.*, vol. 51, edited by B. Evans and T. Wong, pp. 3–31, Elsevier, New York.

Lyakhovsky, V., Y. Bien-Zion, and A. Agnon (1997), Distributed damage, faulting, and friction, *J. Geophys. Res.*, *102*, 27,635–27,649.

Lyakhovsky, V., A. Ilchev, and A. Agnon (2001), Modeling of damage and instabilities of rock mass by means of a nonlinear rheological model, in *Dynamic Rock Mass Response to Mining*, edited by G. Van Aswegen, R. J. Durrheim, and W. D. Ortlepp, pp. 413–420, S. Afr. Inst. of Min. and Metal., Johannesburg.

Mair, K., I. Main, and S. Elphick (2000), Sequential growth of deformation bands in the laboratory, *J. Struct. Geol.*, *22*, 25–42.

Malvern, L. E. (1969), *Introduction to the Mechanics of a Continuum Medium*, Prentice-Hall, Upper Saddle River, N. J.

Menendez, B., W. Zhu, and T. Wong (1996), Micromechanics of brittle faulting and cataclastic flow in Berea sandstone, *J. Struct. Geol.*, *18*, 1–16.

Olsen, M. P., C. H. Scholz, and A. Leger (1998), Healing and sealing of a simulated fault gouge under hydrothermal conditions: Implications for fault healing, *J. Geophys. Res.*, *103*, 7421–7430.

Olsson, W. A. (1999), Theoretical and experimental investigation of compaction bands in porous rock, *J. Geophys. Res.*, *104*, 7219–7228.

Place, D., and P. Mora (2000), Numerical simulation of localization phenomena in a fault zone, *Pure Appl. Geophys.*, *157*, 1821–1845.

Poliakov, A., P. Cundall, Y. Podladchikov, and V. Lyakhovsky (1993), An explicit inertial method for the simulation of viscoelastic flow: An evaluation of elastic effects on diapiric flow in two- and three-layers model, in *Proceedings of the NATO Advanced Study Institute on Dynamic Modeling and Flow in the Earth and Planets*, edited by K. E. Runcorn and D. Stone, pp. 175–195, Springer, New York.

Ricard, Y., and D. Bercovici (2003), Two-phase damage theory and crustal rock failure: The theoretical "void" limit, and the prediction of experimental data, *Geophys. J. Int.*, *155*, 1057–1064.

Rutqvist, J., Y.-S. Wu, C.-F. Tsang, and G. Bodvarsson (2002), A modeling approach for analysis of coupled multiphase fluid flow, heat transfer, and deformation in fractured porous rock, *Int. J. Rock Mech. Min. Sci.*, *39*, 429–442.

Shao, J. F. (1998), Poroelastic behavior of brittle rock materials with anisotropic damage, *Mech. Mater.*, *30*, 41–53.

Tang, C. A., L. G. Tham, P. K. K. Lee, T. H. Yang, and L. C. Li (2002), Coupled analysis of flow, stress and damage (FSD) in rock failure, *Int. J. Rock Mech. Min. Sci.*, *39*, 477–489.

Tenthorey, E., S. F. Cox, and H. F. Todd (2003), Evolution of strength recovery and permeability during fluid-rock in experimental fault zones, *Earth Planet. Sci. Lett.*, *206*, 161–172.

Wong, T., and W. Zhu (1999), Brittle faulting and permeability evolution: Hydromechanical measurement, microstructural observation, and network modeling, in *Faults and Subsurface Fluid Flow in the Shallow Crust*, *Geophys. Monogr. Ser.*, vol. 113, edited by W. C. Haneberg et al., pp. 83–99, AGU, Washington, D. C.

Wong, T., C. David, and W. Zhu (1997), The transition from brittle faulting to cataclastic flow in porous sandstones: Mechanical deformation, *J. Geophys. Res.*, *102*, 3009–3025.

Zhang, J., T. Wong, and D. M. Davies (1990), Micromechanics of pressure-induced grain crushing in porous rocks, *J. Geophys. Res.*, *95*, 341–352.